




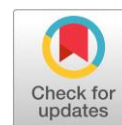


Comparative characteristics of Bi- and La- doped (Ca/Sr)MoO₄-based materials with a defect scheelite-type structure

Zoya A. Mikhaylovskaya ^a , Alexandra V. Klimova ^{b*} , Sofia A. Petrova ^c ,
Elizaveta A. Pankrushina ^a , Elena S. Buyanova ^b 

a: Zavaritsky Institute of Geology and Geochemistry, Ural Branch of the Russian Academy of Sciences, Ekaterinburg 620110, Russia
b: Institute of Natural Sciences and Mathematics, Ural Federal University, Ekaterinburg 620026, Russia
c: Institute of Metallurgy, Ural Branch of the Russian Academy of Sciences, Ekaterinburg 620016, Russia
* Corresponding author: a.v.klimova@urfu.ru



This paper belongs to a Regular Issue.

Abstract

CaMoO₄- and SrMoO₄-based scheelite-type phases are noteworthy functional materials, whose properties strongly correlate with their structure. This work is devoted to La- or Bi-doped scheelite-type molybdates. The purpose of the present study is to quantify the effect of isolated electron pairs of bismuth on the distortion of the structure and related properties. Conventional solid-state technology was used for the synthesis of (Ca/Sr)_{1-3x}La_{2x}Φ_xMoO₄ and Sr_{1-3x}Bi_{2x}Φ_xMoO₄, (0.025 ≤ x ≤ 0.275). The structure was investigated by X-ray powder diffraction and Raman spectroscopy. Rates of structure distortion were characterised by the analysis of the autocorrelation function (AAF) of Raman spectra. Energy gaps were calculated by the Kubelka-Munk method. The conductivity was studied with a.c. impedance spectroscopy. For (Ca/Sr)_{1-3x}(Bi/La)_{2x}Φ_xMoO₄ series 0.025 ≤ x ≤ 0.15 compositions show a basic defect scheelite structure, while 0.15 < x ≤ 0.225 compositions of Bi-doped samples exhibit tetragonal supercells. The chemical compression of unit cell is more evident in the case of Bi-doping, indicating the preferred orientation of the isolated electron pairs. The distortion of MoO₄ polyhedra showed by AAF was more significant for Sr_{1-3x}Bi_{2x}Φ_xMoO₄ than for Sr_{1-3x}La_{2x}Φ_xMoO₄, the Δcorr parameters for Bi-doped compositions were almost double in comparison with La-doped one in the range of 50–600 cm⁻¹ of the Raman shift. The «critical» x = 0.15 point was also clearly indicated by Δcorr parameter. The AAF of the Raman spectra of solid oxides was shown to be a good tool for prediction of properties and points of phase transitions in solid oxides.

Keywords

strontium bismuth molybdate
calcium bismuth molybdate
X-ray diffraction
Raman spectroscopy
autocorrelation function
conductivity
energy gap

Key findings

- The AAF demonstrated that the isolated electron pair of bismuth plays a key role in the distortion of the Mo–O sublattice.
- The decrease in the calculated energy gap with increasing x-value is observed both for the (Ca/Sr)_{1-3x}La_{2x}Φ_xMoO₄ and Sr_{1-3x}Bi_{2x}Φ_xMoO₄ systems.
- In contrast to Sr_{1-3x}Bi_{2x}Φ_xMoO₄ compositions, (Ca/Sr)_{1-3x}La_{2x}Φ_xMoO₄ show the general decrease of conductivity.

Received: 20.10.23

Revised: 17.11.23

Accepted: 27.11.23

Available online: 06.12.23

© 2023, the Authors. This article is published in open access under the terms and conditions of the Creative Commons Attribution (CC BY) license (<http://creativecommons.org/licenses/by/4.0/>).

1. Introduction

In recent years, CaMoO₄-based and SrMoO₄-based phases have attracted interest in many technological fields because of a broad range of applications. For example, such materials can be used in catalytic systems, such as photocatalysts

and pigments [1, 2], ionic conductors, microwave devices [3, 4–7], photoluminescent devices [3, 8–10], etc. [1–10]. Usually CaMoO₄ and SrMoO₄-based phases show scheelite-type structure, and properties of these complex oxides are strongly correlated with the nature and concentration of dopants [3, 7–10].

One of the most popular ways of modifying the properties of the (Ca/Sr)MoO₄ systems is A site doping by trivalent Me³⁺ cations [3, 4, 7–9, 11, 12]. It can be realised in following ways:

1) formation of (A_{1-x}M_xBO_{4+x/2}) solid solutions as in works [8, 12, 13];

2) co-substitution in A or B sites by subvalent cations forming A_{1-2x}Me³⁺_xMe⁵⁺_xBO₄ or A_{1-x}Me³⁺_xB_{1-x}Me⁵⁺_xO₄ solid solutions, respectively [7];

3) formation of cation vacancies (A_{1-3x}M_{2x}Φ_xBO₄) [11, 12].

In the present work the third way was used. We studied (Ca/Sr)_{1-3x}La_{2x}Φ_xMoO₄ solid solutions in comparison with the (Ca/Sr)_{1-3x}Bi_{2x}Φ_xMoO₄ solid solutions, where Φ is the cation vacancy. The limiting cases of such systems are CaMoO₄ or SrMoO₄ with an ideal scheelite structure and (La/Bi)_{2/3}MoO₄ with a highly distorted scheelite structure [14]. Ca_{1-3x}Bi_{2x}Φ_xMoO₄ and Sr_{1-3x}Bi_{2x}Φ_xMoO₄ were investigated in the previous works [11, 15–17]. The (Ca/Sr)_{1-3x}Bi_{2x}Φ_xMoO₄ compounds were first described by Sleight and Aykan [15] for the $x = 0.04$ compositions in the (Ca/Sr)_{1-3x}Bi_{2x}Φ_xMoO₄ systems. They exhibit the tetragonal scheelite structure. Guo et al. [11, 16] synthesized compositions in the Ca_{1-3x}Bi_{2x}Φ_xMoO₄ system in the range $0.005 \leq x \leq 0.20$ and examined their microstructures and microwave dielectric properties. The $0.00 \leq x \leq 0.15$ compositions were single-phase and had the tetragonal scheelite structure with cationic vacancies. The $x = 0.2$ composition was reported to contain a second unidentified phase. Vibrational spectroscopy results revealed large distortions of MoO₄ and BiO₈ polyhedra [11] with a strong correlation between the A site substitution and the microwave dielectric properties. In later works, additional peaks identified by Guo et al. in the compositions of Ca_{1-3x}Bi_{2x}Φ_xMoO₄ above $x = 0.15$ could be indexed in the tetragonal supercell with $a_{\text{sup}} \approx \sqrt{5}a$, $c_{\text{sup}} \approx c$ (where a and c are the tetragonal scheelite cell parameters) [16–18]. This superstructure was evident throughout the compositional range $0.15 < x \leq 0.225$ and was caused by bismuth ions ordering. The electrical conductivity and the photocatalytic activity of Ca_{1-3x}Bi_{2x}Φ_xMoO₄ were found to be higher in the samples with higher Bi content [17]. In contrast, the electrical conductivity and photocatalytic activity of Sr_{1-3x}Bi_{2x}Φ_xMoO₄ has not been reported yet, and there are no vibrational spectroscopy data for such compounds.

La_{2/3}MoO₄ (La₂Mo₃O₁₂) and Bi_{2/3}MoO₄ (Bi₂Mo₃O₁₂) were also reported as conductors [19, 20] and luminescent materials [21]. La_{2/3}MoO₄ and Bi_{2/3}MoO₄ molybdates represent different structural variants that exist in the defect scheelite. Both structure types are characterized by a unique ordering of the trivalent cations and cation vacancies [22]. Bi_{2/3}MoO₄ (space group P2₁/c) contains three scheelite subcells per unit cell, which include tetrahedral pairs of [Mo₂O₈] groups [23]. This specific ordering is driven by the asymmetric nature of the Bi³⁺ cation with its directionally oriented lone pair of electrons, resulting from similar ionic radii of Bi³⁺ and La³⁺ [22]. In contrast to Bi³⁺, the asymmetry for La³⁺ cations is absent from the La_{2/3}MoO₄ (space group C2/c). Therefore, in the case of (Ca/Sr)_{1-3x}(Bi/La)_{2x}Φ_xMoO₄

solid solutions the lone electron pair effect of Bi³⁺ is expected to impact the structure and properties of these compounds [22].

Here we present a study of the (Ca/Sr)_{1-3x}La_{2x}Φ_xMoO₄ system in comparison with Sr_{1-3x}Bi_{2x}Φ_xMoO₄ system, which also might be expected to be a promising ionic conductor, catalyst, dielectric material, etc. The structural features were examined using X-ray diffraction and Raman spectroscopy. The autocorrelation function analysis was used to examine trends in similar samples of Bi- and La-doped strontium molybdates. The decreasing trend in the energy gap values calculated using the Kubelka-Munk method and UV-Vis spectroscopy was shown. The conductive properties of doped strontium molybdates were examined by impedance spectroscopy.

2. Experimental

Compositions of the general formula (Ca/Sr)_{1-3x}La_{2x}Φ_xMoO₄ and Sr_{1-3x}Bi_{2x}Φ_xMoO₄, ($0.025 \leq x \leq 0.275$) series were synthesized by a conventional solid state method [18] from SrCO₃ (99.0%, Reakhim), Bi₂O₃ (99.9%, Merck), La₂O₃ (99.9%, Merck) and MoO₃ (99.5%, Reakhim) in the range of 600–900 °C and 500–700 °C respectively. The density of the homogeneous powders (ρ_{exp}) was determined using 2 ml pycnometers with distilled water as the displacement liquid.

X-ray powder diffraction data were obtained using a Bruker Advance D8 diffractometer with a VANTEC1 detector (Ni filtered Cu K α radiation, θ/θ geometry) in Ural-M center of Institute of Metallurgy. The data were collected in the 2θ range of 6–120°, in steps of 0.02103° with an effective scan time of 200 s per step.

Raman spectra were obtained for Sr_{1-3x}(Bi/La)_{2x}Φ_xMoO₄ series with a Horiba LabRam HR800 Evolution spectrometer equipped with an Olympus BX-FM confocal microscope (50 \times objective, numerical aperture = 0.7) and He-Ne laser (radiation wavelength 633 nm) and 600 gr/mm grating. The spectral resolution was about 1 cm⁻¹, and the spatial lateral resolution was about 2 μm . The spectra were fitted using a Gaussian-Lorentzian model. The UV-Vis spectra were obtained in the range 350–1100 nm using a Thermo Scientific Evolution 300 spectrophotometer equipped with an integrating sphere. Energy gaps for direct inter-band transitions were calculated by linear approximation of the Kubelka-Munk function [24]. The a.c. impedance spectra were obtained with an Elins Z-3000 impedancemeter for ceramic samples of (Ca/Sr)_{1-3x}La_{2x}Φ_xMoO₄ and Sr_{1-3x}Bi_{2x}Φ_xMoO₄ with platinum electrodes.

3. Results and Discussions

Figure 1 shows the X-ray diffraction patterns of representative compositions in the Ca_{1-3x}La_{2x}Φ_xMoO₄ and Sr_{1-3x}La_{2x}Φ_xMoO₄ systems. In the compositional range $0 \leq x \leq 0.15$, the patterns of (Ca/Sr)_{1-3x}La_{2x}Φ_xMoO₄ can be indexed using a tetragonal scheelite model in the space group I4₁/a with no additional reflections.

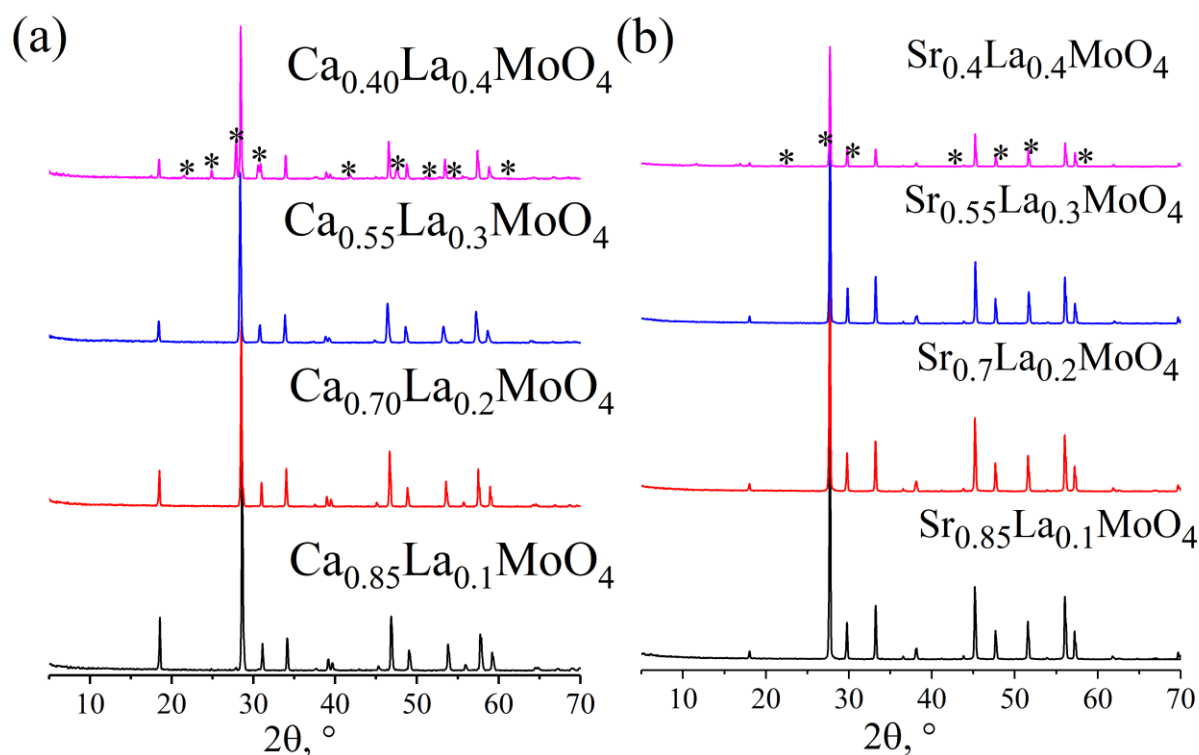


Figure 1 Detail of X-ray diffraction patterns of selected compositions of the $(\text{Ca/Sr})_{1-3x}\text{La}_{2x}\Phi_x\text{MoO}_4$ systems. Peaks of $\text{La}_2\text{Mo}_3\text{O}_{12}$ are marked with asterisks.

XPRD patterns of $x \geq 0.2$ compositions contain reflections of $(\text{Ca/Sr})\text{MoO}_4$ and $\text{La}_2\text{Mo}_3\text{O}_{12}$ phases. In the $\text{Sr}_{1-3x}\text{Bi}_{2x}\Phi_x\text{MoO}_4$ system ($0 \leq x \leq 0.125$), the patterns were indexed using a tetragonal scheelite model, while the patterns for the ($0.125 \leq x \leq 0.225$) compositions were indexed using a superstructured scheelite model ($a_{\text{sup}} = \sqrt{5}a_{\text{sub}}$, $c_{\text{sup}} = c_{\text{sub}}$), as in the previous studies [17, 18].

The compositional dependence of the unit cell parameters is shown in Figure 2. A general decrease in the unit cell parameters is observed over the compositional range studied, which is attributable to the substitution of Sr^{2+} by smaller Bi^{3+} and La^{3+} cations with ionic radii of 1.26, 1.17 Å and 1.16 Å, respectively [25]. The opposite correlation is observed for Ca^{2+} replaced with Bi^{3+} and La^{3+} cations: due to its smaller ionic radius of 1.12 Å [25] the unit cell parameters generally increase. Two linear ranges for both basic and superstructured complex oxides are observed for the Bi-doped compositions. For $\text{Ca}_{1-3x}\text{La}_{2x}\Phi_x\text{MoO}_4$ and $\text{Sr}_{1-3x}\text{La}_{2x}\Phi_x\text{MoO}_4$ no additional ordering was observed, and there is only one linear range on the graphs. The chemical compression of the unit cell of bismuth-substituted SrMoO_4 is more significant than that in the case of doping by lanthanum. This indicates that the average ionic radii of bismuth can be less than 1.17 Å, probably due to the preferred orientation of $6s^2$ electronic pair of bismuth. The measured densities are in good agreement with the theoretical values calculated from the X-ray data (within 2%). Bi-doped samples showed the most intensive growth of density with x .

Changes of structure of Bi- and La-doped strontium molybdates were investigated with Raman spectroscopy. The general compression of unit cell of $\text{Sr}_{1-3x}(\text{Bi/La})_{2x}\Phi_x\text{MoO}_4$

results in more evident distortion of the structure fragments, whereas the general expansion of $\text{Ca}_{1-3x}\text{La}_{2x}\Phi_x\text{MoO}_4$ can result in a minimisation of the distortion. The recorded Raman spectra are shown in Figure 3. The lattice vibrations in the scheelite-structured compounds include internal modes that correspond to vibrations inside the $[\text{MoO}_4]^{2-}$ tetrahedra and external modes that are assigned to lattice vibrations. Because of crystal field effects and Davydov splitting, the degeneracy of the $[\text{MoO}_4]^{2-}$ vibrations corresponding to T_d symmetry in free space is resolved.

The group theoretical analysis predicts that 26 modes are possible in the case of tetragonal scheelite-structured compounds in space group $I4_1/a$, which are distributed as irreducible representations [26–28]: $\Gamma = 3A_g + 5B_g + 5E_g + 5A_u + 3B_u + 5E_u$, of which the A_g , B_g and E_g vibrations are Raman active, whereas the A_u , B_u and E_u vibrations are infrared active. In the present study, 13 vibrational modes are observed for the end member SrMoO_4 , which is in good agreement with previous experimental and calculated results for this composition [26–28]. According to the previous studies, the modes in the low-frequency range of spectra (modes 1–6 in Figure 3) correspond to the external modes of O–Mo–O and O–Sr–O bands [29–31], while medium and high frequency ranges contain internal vibrations (modes 7–13 in Figure 3). The Mo–O bending modes are found to be located at medium frequencies (ν_2 and ν_4 , modes 7–10) while the Mo–O stretching modes are detected at high frequencies (ν_1 and ν_3 , modes 11–13) [27–29, 11].

Doping of strontium molybdates with Bi^{3+} and La^{3+} leads to a broadening of peaks in the Raman spectrum and the appearance of additional modes.

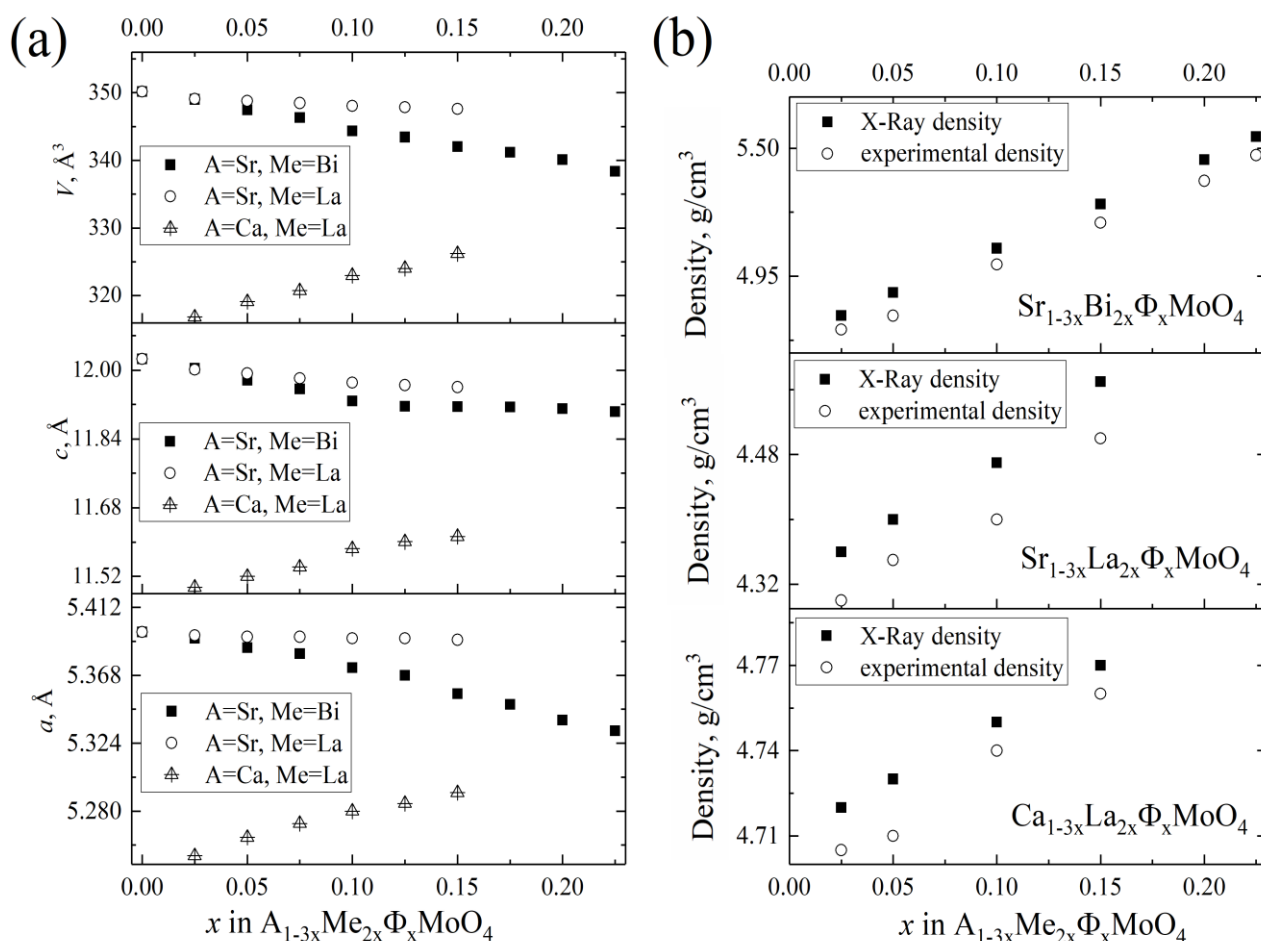


Figure 2 Unit cell parameters, unit cell volume (a), calculated and measured densities (b) of $(\text{Ca}/\text{Sr})_{1-3x}\text{Me}_{2x}\Phi_x\text{MoO}_4$ and $\text{Sr}_{1-3x}\text{Bi}_{2x}\Phi_x\text{MoO}_4$ compositions. For $x=0.15\dots0.225$ compositions of $\text{Sr}_{1-3x}\text{Bi}_{2x}\Phi_x\text{MoO}_4$ series subcell values are shown ($a' = a/\sqrt{5}$, $V' = V/5$).

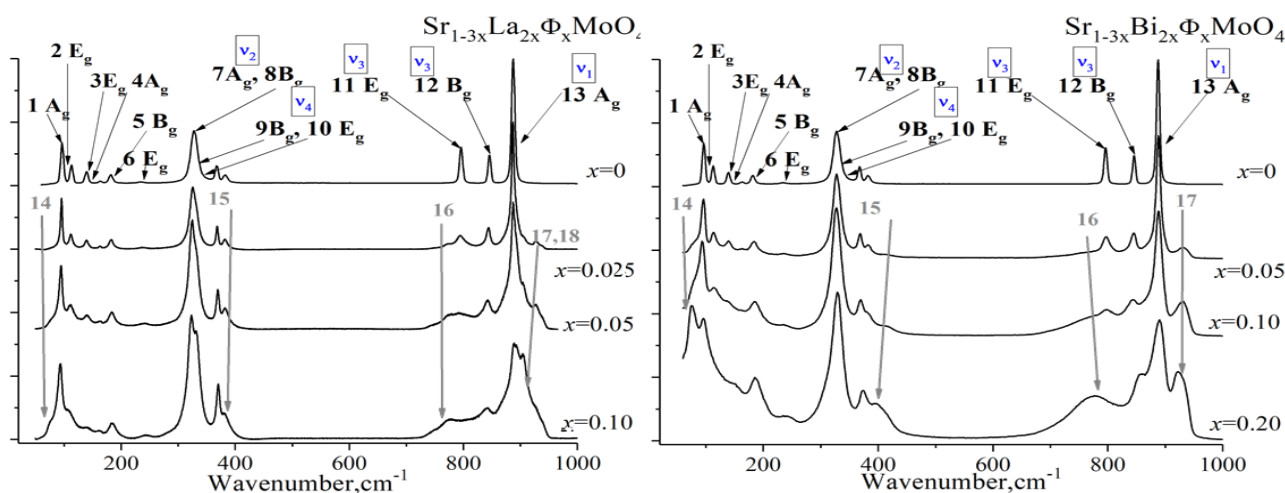


Figure 3 Raman spectra of selected compositions in the $\text{Sr}_{1-3x}\text{Bi}_{2x}\Phi_x\text{MoO}_4$ and $\text{Sr}_{1-3x}\text{La}_{2x}\Phi_x\text{MoO}_4$ systems. Additional modes are shown in grey color.

The following additional modes were detected: “mode-14” at 80–87 cm^{-1} , “mode-15” at 406–412 cm^{-1} , “mode-16” at 770–790 cm^{-1} and “mode-17 and 18” at 925–932 cm^{-1} . Modes-14-16 are probably associated with distorted MoO_4 tetrahedra as it was suggested by Guo et al. [11] in the case of $\text{Ca}_{1-3x}\text{Bi}_{2x}\Phi_x\text{MoO}_4$ system. The modes-17 and 18 have been previously detected for SrMoO_4 at high pressure (12 GPa) [30], where SrMoO_4 had a distorted scheelite structure, and these modes were also associated with ν_1 Mo–O stretching

vibrations. In this work chemical compression of the unit cell can result a similar distortion of MoO_4 polyhedra. Hence “mode-17” and “mode-18” can be also ascribed to a short Mo–O bond vibration.

Unfortunately, the compositional variations of these modes and the full width at half maximum (FWHM) are not absolutely clear because of significant broadening of the peaks.

Figure 4 shows the examples of peak fitting for several compositions, indicating a high overlap of spectral lines.

We can only point out the general increasing trend of FWHM values with increasing x -value. This indicates a variation in the length of Mo–O bonds, but a correct direct quantitative analysis is impossible. That is why we used an analysis of autocorrelation function (AAF). Salje et al. [31] proposed an autocorrelation function $\text{Corr}(\alpha, \omega')$ as a way of parametrizing effective line widths in IR spectra in order to examine trends in similar samples. The AAF method was later adapted for examining Raman spectra by Pankrushina et al. [32]. $\text{Corr}(\alpha, \omega')$ can be calculated using Equation 1:

$$\text{Corr}(\alpha, \omega') = \int_{-\infty}^{\infty} \alpha(\omega + \omega')\alpha(\omega)d\omega, \quad (1)$$

where $\alpha(\omega)$ is the primary spectrum and $\alpha(\omega + \omega')$ is a replica of the spectrum shifted by ω' .

Salje et al. [31] calculated the Δcorr parameter as follows: the background was subtracted from the $\alpha(\omega)$ initial spectrum, the $\text{Corr}(\alpha, \omega')$ was calculated and normalised, and then the $\text{Corr}(\alpha, \omega')$ peak apex is approximated by the Gaussian function. The Δcorr parameter is determined by extrapolating the σ function to the $\Delta\omega' = 0$ point using second-order polynomials. In this work a modified Gaussian function [32] was used. Thus, Δcorr is an approximation of the σ parameter of the Gaussian function, which is calculated from the $\text{Corr}(\alpha, \omega')$ peak apex and is proportional to the full widths at half maximum (FWHM) of the autocorrelation function. At the same time, Δcorr is the average estimate of the FWHM of the peaks in the spectrum. In the present work Δcorr was calculated over three frequency ranges (50–250 cm^{-1} , 250–600 cm^{-1} and 600–1000 cm^{-1} , covering

the lattice modes, $\nu_2 + \nu_4$ and $\nu_1 + \nu_3 + \nu_4$, respectively). For all wavenumber ranges, Δcorr (i.e., FWHM values) increases. This indicates a systematic distortion of MoO_4 polyhedra. However, in the case of $\text{Sr}_{1-3x}\text{Bi}_{2x}\Phi_x\text{MoO}_4$ it increases up to $x = 0.15$, and above $x = 0.15$ Δcorr either decreases or changes little. It means that ordering in A-sublattice results the reduction of the distortion of MoO_4 polyhedra. For $\text{Sr}_{1-3x}\text{La}_{2x}\Phi_x\text{MoO}_4$ Δcorr also increases but in general the values of Δcorr is smaller. It indicates that $6s^2$ pair of bismuth is a strong factor of the distortion of molybdenum-oxygen sublattice.

Typical optical diffuse scattering spectra and Tauc plots are shown in Figure 6. The scattering in the range of ~500–1100 nm is close to 100%. The spectrum for SrMoO_4 contains a broad band in the range of 200–300 nm, which corresponds to electronic transitions within the molybdate tetrahedra [33]. In the substituted samples, this band slightly shifts to a higher wavelength (Figure 6). In general, the spectra are similar to those of $(\text{Ca}/\text{Sr})_{1-3x}\text{Bi}_{2x}\Phi_x\text{MoO}_4$ [18]. Band gap (E_g) calculations were performed using the Kublenka-Munk theory and the Tauc relation [24]. The value of E_g can be obtained by interpolating the linear part of the Tauc plots.

Band gap values decreased with increasing x -value (Table 1) for both Bi^{3+} and La^{3+} doping. The conduction band (CB) in SrMoO_4 is formed by Mo 4d states with some mixing of the O 2p states [26, 27], and the Mo 4d states in CB are split by the tetrahedral crystal field into two groups of states, as in other scheelite compounds [26, 27, 34].

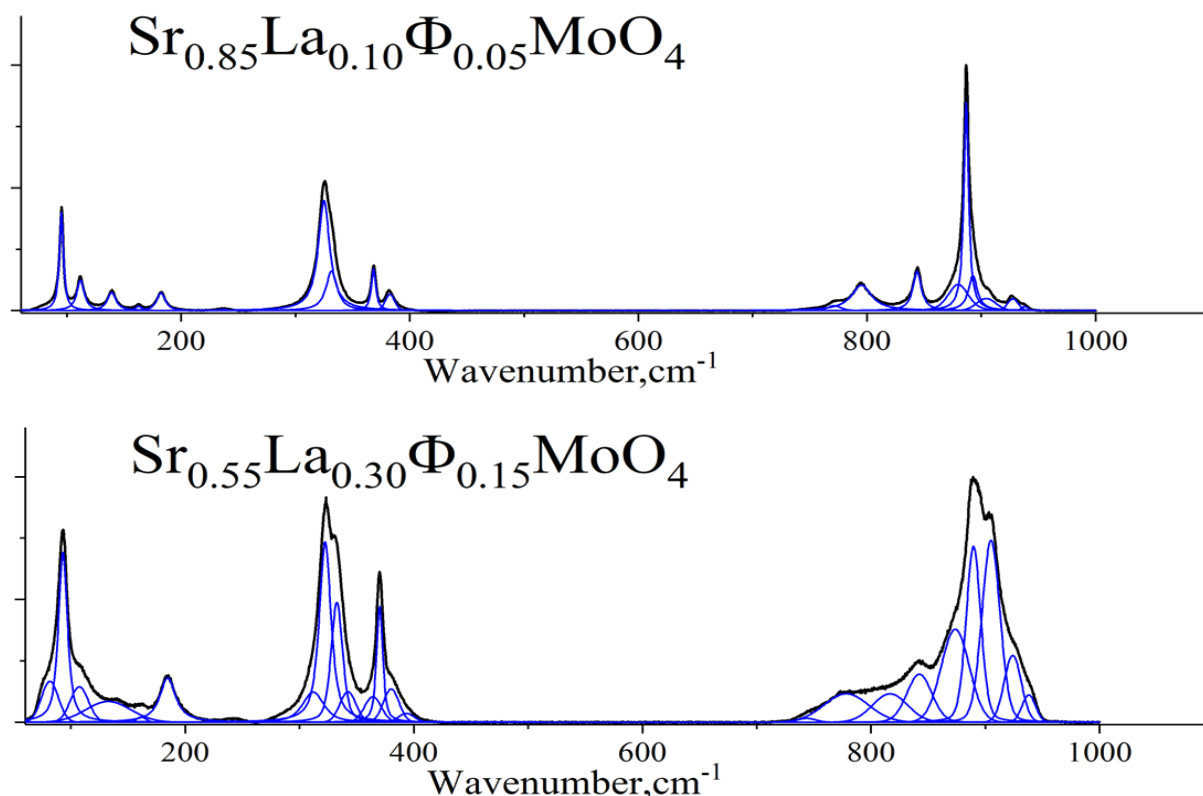


Figure 4 Examples of fitting by Gauss functions are shown for the selected Raman spectra for $\text{Sr}_{1-3x}\text{La}_{2x}\Phi_x\text{MoO}_4$.

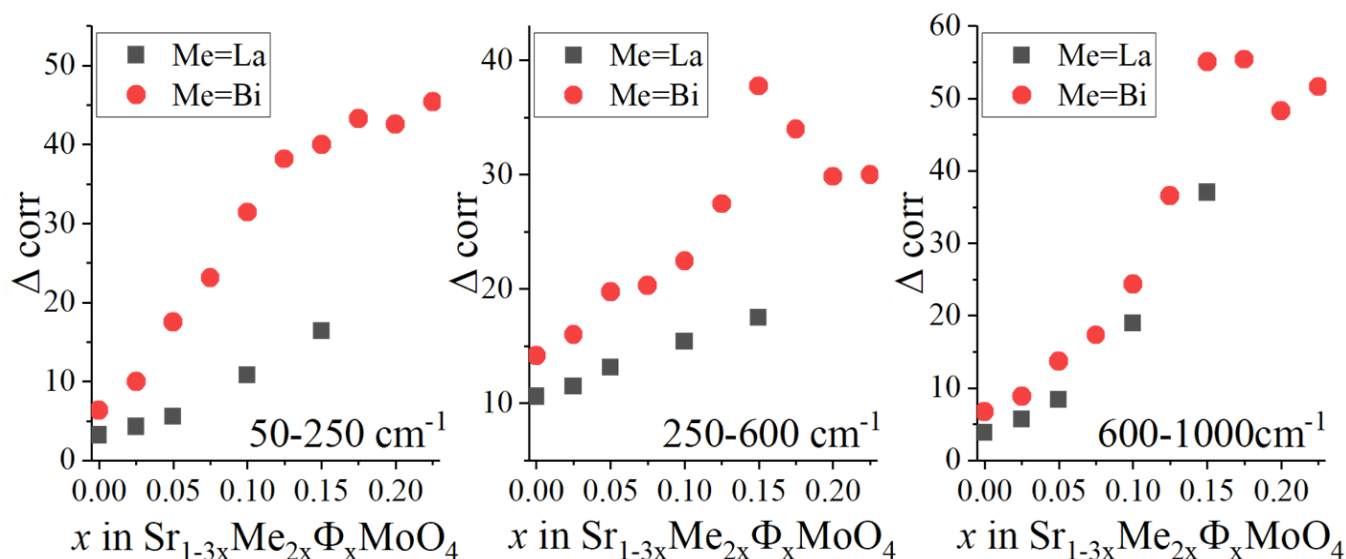


Figure 5 Compositional variation of Δcorr over different frequency ranges.

In the case of doping with Me^{3+} , the splitting of the CB is expected to be absent because of the distortion of the MoO_4 polyhedra. It can also lead to a slight decrease of E_g like in the case of doping by lanthanum (Table 1). In the case of bismuth, the energy gap decreases substantially, probably because of the additional Bi 6p states in the electronic spectra [35]. Such a band gap decrease is favourable for the use of Bi-doped molybdates as yellow pigments or as photocatalysts.

The conductivity of $(\text{Ca}/\text{Sr})_{1-3x}\text{La}_{2x}\Phi_x\text{MoO}_4$ and $\text{Sr}_{1-3x}\text{Bi}_{2x}\Phi_x\text{MoO}_4$ was studied by a.c. impedance spectroscopy in the temperature ranges of 400–900 °C and 400–700 °C, respectively. SrMoO_4 is known to be an ionic conductor with $t_{\text{O}^{2-}}$ close to 1 [36]. The impedance spectra were similar for all compositions over the measurement range, showing semicircles with a zero high frequency intercept on the real axis (Figure 7). The equivalent circuit consists of a parallel combination of a resistor (R) and a capacitor (C), as in the previous work devoted to the molybdates of calcium and strontium [36]. The capacitance value (C) was found to be $\sim 10^{-11}$ F, corresponding to the total impedance of the electrolyte [37]. Separation of the total resistance into bulk and grain boundary components was not possible.

Arrhenius plots of the total conductivity and compositional variation of conductivity at 873 K for the $\text{Sr}_{1-3x}\text{Bi}_{2x}\Phi_x\text{MoO}_4$ series are presented in Figure 8. The Arrhenius plots are generally linear, with a slight deviation from the linearity caused by kinetic restraints at low temperatures. The conductivity of SrMoO_4 is in good agreement with the previous studies [36]. All $\text{Sr}_{1-3x}\text{Bi}_{2x}\Phi_x\text{MoO}_4$ compositions show increased conductivity in comparison to SrMoO_4 .

The activation energy changes insignificantly (from ~ 1.2 to ~ 1.1 eV for $\text{Ca}_{1-3x}\text{La}_{2x}\text{MoO}_4$, from ~ 0.8 to 0.85 eV for $\text{Ca}_{1-3x}\text{Bi}_{2x}\text{MoO}_4$ and from ~ 1.30 to 1.41 for $\text{Sr}_{1-3x}\text{La}_{2x}\text{MoO}_4$), indicating that the conduction mechanism in doped molybdates in general is similar to that in the parent compounds [16].

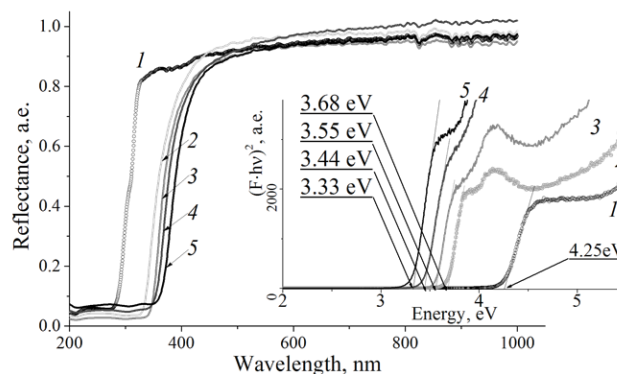


Figure 6 Optical diffuse scattering spectra for selected compositions in the $\text{Sr}_{1-3x}\text{Bi}_{2x}\Phi_x\text{MoO}_4$ system and corresponding Tauc plots (at inset): 1 – SrMoO_4 ; 2 – $x = 0.05$; 3 – $x = 0.10$; 4 – $x = 0.15$; 5 – $x = 0.20$.

Table 1 Compositional variation of optical band gap (E_g direct) in the $\text{A}_{1-3x}\text{Me}_{2x}\Phi_x\text{MoO}_4$, A = Ca/Sr, Me = Bi/La [17, 18].

x	0.05	0.075	0.10	0.125	0.15	0.175	0.2
A = Sr, Me = Bi;	3.68	3.61	3.55	3.48	3.44	3.40	3.33
E_g , eV							
A = Ca, Me = La;	3.90	3.87	3.84	3.80	3.75	-	-
E_g , eV							
A = Sr, Me = La;	4.17	4.11	4.08	3.96	3.89	-	-
E_g , eV							

However, there can be a change in the transference number, with a greater electronic contribution to conductivity. Ionic transport in scheelite-type compounds assumes the presence of irregular interstitial oxygen positions, although these have not been identified using diffraction methods [12]. Therefore, conductivity can be induced by increasing the number of such positions due to the distortion of MoO_4 polyhedra. On the other hand, in scheelite-type compounds additional n -type transfer can be realised [38].

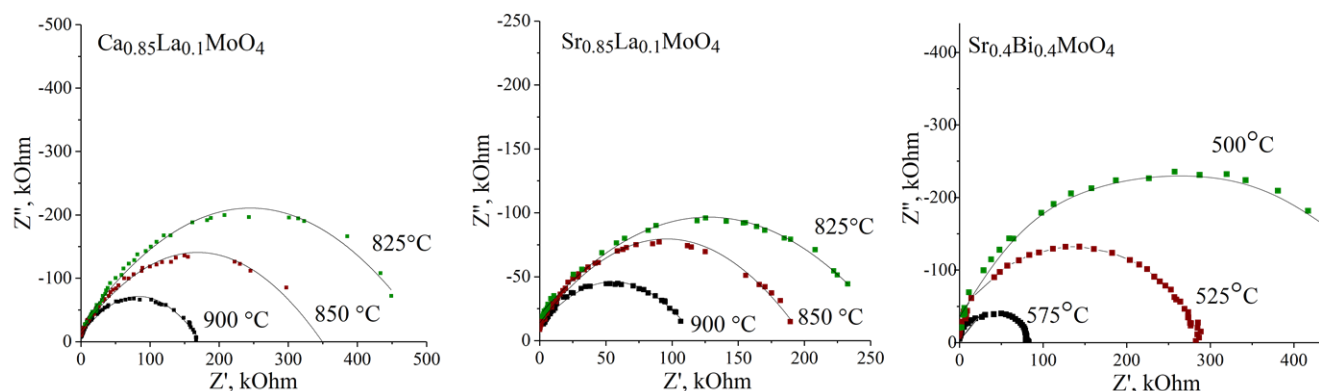


Figure 7 A typical impedance spectrum of $(\text{Ca}/\text{Sr})_{1-3x}\text{La}_{2x}\Phi_x\text{MoO}_4$ and $\text{Sr}_{1-3x}\text{Bi}_{2x}\Phi_x\text{MoO}_4$ systems at different temperatures.

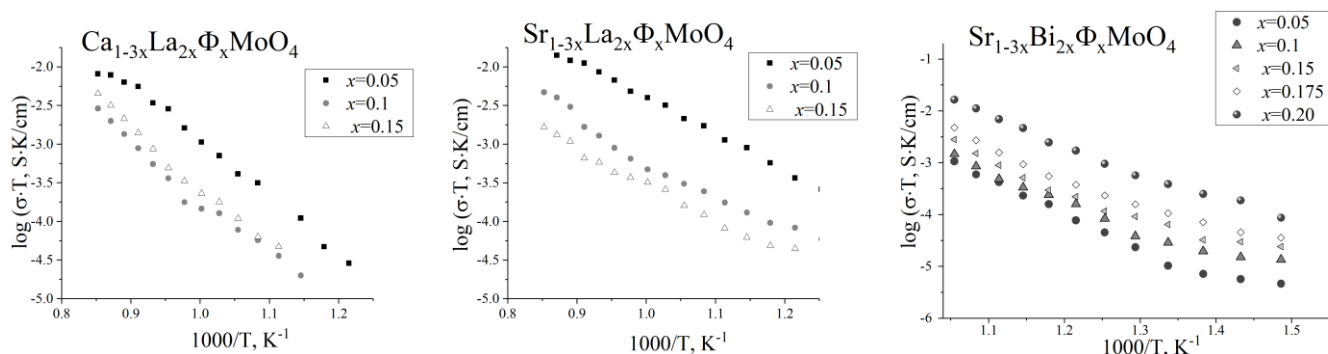


Figure 8 Arrhenius plots of total conductivity for $(\text{Ca}/\text{Sr})_{1-3x}\text{La}_{2x}\Phi_x\text{MoO}_4$ and $\text{Sr}_{1-3x}\text{Bi}_{2x}\Phi_x\text{MoO}_4$ complex oxides.

In the case of $\text{Sr}_{1-3x}\text{Bi}_{2x}\Phi_x\text{MoO}_4$ the n -type electronic contribution can be caused by the presence of low concentrations of reduced molybdenum species at the grain surfaces, namely Mo^{4+} and Mo^{5+} ions. The maximum values of total conductivity at 948 K were $1.75 \cdot 10^{-5} \text{ S}\cdot\text{cm}^{-1}$ and $2.82 \cdot 10^{-5} \text{ S}\cdot\text{cm}^{-1}$ for the $x = 0.200$ and $x = 0.225$ compositions, respectively, which is less than the conductivity of $\text{Bi}_2\text{Mo}_3\text{O}_{12}$ under the same conditions [39]. In contrast to $\text{Sr}_{1-3x}\text{Bi}_{2x}\Phi_x\text{MoO}_4$ compositions $(\text{Ca}/\text{Sr})_{1-3x}\text{La}_{2x}\Phi_x\text{MoO}_4$ show the general decrease of conductivity (Figure 8). Probably, this decrease in conductivity is due to either the smaller distortion of molybdenum-oxygen polyhedra, which causes the decrease of oxygen ion mobility, or the lower concentrations of reduced molybdenum species at the grain surfaces of $(\text{Ca}/\text{Sr})_{1-3x}\text{La}_{2x}\Phi_x\text{MoO}_4$ as compared with $\text{Sr}_{1-3x}\text{Bi}_{2x}\Phi_x\text{MoO}_4$. The maximum values of the total conductivity at 948 K among $(\text{Ca}/\text{Sr})_{1-3x}\text{La}_{2x}\Phi_x\text{MoO}_4$ were $4.34 \cdot 10^{-7} \text{ S}\cdot\text{cm}^{-1}$ and $2.25 \cdot 10^{-6} \text{ S}\cdot\text{cm}^{-1}$ for the doped calcium molybdate and strontium molybdate, respectively.

4. Limitations

In this work, the synthesis is highly sensitive to the purity of molybdenum oxide, the insufficient purity of which leads to the formation of non-single-phase samples. Lanthanum oxide should be weighed immediately after annealing at a temperature of at least 1000 °C because lanthanum oxide strongly absorbs H_2O and CO_2 .

Bismuth oxide can evaporate during synthesis, which leads to a change in the chemical composition. The chemical composition of compounds can be confirmed by dissolving

samples and analyzing them using AES; however, this data were not included in this work. In this study, we were not able to determine the exact oxidation state of molybdenum, so it was taken as Mo^{+6} , since Mo^{+5} is often present in a low concentration on the surface of bismuth molybdates. The maximum frequency measured with the Elins Z-3000 impedancemeter is 1000 kHz. Approximation of spectra by AAF using the Gaussian-Lorentzian model significantly slows down the calculation; therefore, we used the Gaussian model. The diffuse scattering spectra of these complex oxides are very sensitive to sample preparation, e.g. texturing or a small amount of sample leads to large noises.

5. Conclusions

Thus, in the present work, the synthesis of $(\text{Ca}/\text{Sr})\text{MoO}_4$ doped by La and Bi (what are ions with a close radii) was carried out. A comparative study of their structure and properties was conducted. The results of the investigation of the structure and properties of $(\text{Ca}/\text{Sr})_{1-3x}\text{La}_{2x}\Phi_x\text{MoO}_4$ and $\text{Sr}_{1-3x}\text{Bi}_{2x}\Phi_x\text{MoO}_4$ are consistent with those of the previous studies [11, 16–18]. Bi^{3+} and La^{3+} ions possess similar ionic radii; however, the $6s^2$ isolated electron pair of bismuth was shown to be a significant factor in the regulation of structure and properties. A cation vacancy solid solution is formed in the system $\text{Sr}_{1-3x}\text{La}_{2x}\Phi_x\text{MoO}_4$ over the compositional range $0.0 \leq x \leq 0.15$. Phases of $(\text{Ca}/\text{Sr})_{1-3x}\text{La}_{2x}\Phi_x\text{MoO}_4$ and $\text{Sr}_{1-3x}\text{Bi}_{2x}\Phi_x\text{MoO}_4$ in the range $0.025 \leq x \leq 0.15$ show a tetragonal scheelite structure, isostructural with SrMoO_4 , while in the range $0.15 < x \leq 0.225$ a tetragonal superstruc-

ture is seen for the phases of $\text{Sr}_{1-3x}\text{Bi}_{2x}\Phi_x\text{MoO}_4$. Strong distortion of the MoO_4 polyhedra in $(\text{Ca}/\text{Sr})_{1-3x}\text{La}_{2x}\Phi_x\text{MoO}_4$ and $\text{Sr}_{1-3x}\text{Bi}_{2x}\Phi_x\text{MoO}_4$ was seen in the crystal structure and reflected in the Raman spectra. Using AAF, we demonstrated quantitatively that the isolated electron pair of bismuth plays a key role in the distortion of the Mo–O sublattice. It means that the AAF of the Raman spectra of series of complex oxides can also be used to predict their conductive properties. The Δ_{corr} parameter confirmed the $x = 0.15$ composition to be a “critical” point for $\text{Sr}_{1-3x}\text{Bi}_{2x}\Phi_x\text{MoO}_4$. It indicates a strong change in the structure of $0.15 \leq x \leq 0.225$ compositions caused by bismuth ordering and less distorted MoO_4 polyhedra. The Δ_{corr} parameter also showed smaller distortion in the case of doping with lanthanum, indicating the significant effect of $6s^2$ isolated electron pair of bismuth. As a result, the conductivity increases with increasing Bi content and decreases with La content. Thus, AAF was shown to be an effective tool to find “critical” points among series of solid solutions.

The decrease of calculated energy gap with increasing x -value is observed both in $(\text{Ca}/\text{Sr})_{1-3x}\text{La}_{2x}\Phi_x\text{MoO}_4$ and $\text{Sr}_{1-3x}\text{Bi}_{2x}\Phi_x\text{MoO}_4$ systems. In the case of bismuth, the energy gap decreases substantially, probably, because of additional the Bi 6p states in electronic spectra. Such a band gap decrease is favorable for using of Bi-doped molybdates as yellow pigments or as photocatalysts. Conductivity increases with increasing x -value in the $\text{Sr}_{1-3x}\text{Bi}_{2x}\Phi_x\text{MoO}_4$ system and decreases in the case of $(\text{Ca}/\text{Sr})_{1-3x}\text{La}_{2x}\Phi_x\text{MoO}_4$ system, also indicating the effect of $6s^2$ isolated electron pair of bismuth. A maximum value of $2.82 \cdot 10^{-5} \text{ S}\cdot\text{cm}^{-1}$ was achieved at 948 K for the $x = 0.255$ composition. The maximum values of the total conductivity among all $(\text{Ca}/\text{Sr})_{1-3x}\text{La}_{2x}\Phi_x\text{MoO}_4$ at 948 K were $4.34 \cdot 10^{-7} \text{ S}\cdot\text{cm}^{-1}$ and $2.25 \cdot 10^{-6} \text{ S}\cdot\text{cm}^{-1}$ for the doped calcium molybdate and strontium molybdate, respectively.

• Supplementary materials

No supplementary materials are available.

• Funding

This work was fulfilled as part of the Government task to the Institute of Geology and Geochemistry (theme No. AAAA-A19-119071090011-6). The retrofit and development of the Geoanalytik Shared Facilities Center of the Institute of Geology and Geochemistry is carried out under a grant from the Ministry of Higher Education and Science of the Russian Federation (agreement No. 075-15-2021-680).

• Acknowledgments

The XRD data were obtained in Ural-M center of Institute for Metallurgy, Ural Branch of RAS, the Raman data were obtained in Geoanalytik center of Zavaritsky Institute of Geology and Geochemistry, Ural Branch of RAS.

• Author contributions

Conceptualization: Z.A.M., E.S.B.
 Data curation: Z.A.M., E.S.B., E.A.P.
 Formal Analysis: E.S.B., Z.A.M.
 Funding acquisition: Z.A.M.
 Investigation: Z.A.M., A.V.K., S.A.P., E.A.P.,
 Methodology: Z.A.M., E.A.P., S.A.P.
 Project administration: Z.A.M.
 Resources: E.S.B.
 Software: E.S.B., E.A.P.
 Supervision: Z.A.M.
 Validation: E.S.B.
 Visualization: Z.A.M., E.S.B.
 Writing – original draft: Z.A.M.
 Writing – review & editing: Z.A.M., E.S.B., A.V.K.

• Conflict of interest

The authors declare no conflict of interest.

• Additional information

Author IDs:

Zoya A. Mikhaylovskaya, Scopus ID [26536460700](https://scopus.com/authid/detail.url?authorID=26536460700);
 Alexandra V. Klimova, Scopus ID [57223927579](https://scopus.com/authid/detail.url?authorID=57223927579);
 Sofia A. Petrova, Scopus ID [7006291101](https://scopus.com/authid/detail.url?authorID=7006291101);
 Elizaveta A. Pankrushina, Scopus ID [57204032915](https://scopus.com/authid/detail.url?authorID=57204032915);
 Elena S. Buyanova, Scopus ID [26536460700](https://scopus.com/authid/detail.url?authorID=26536460700).

Websites:

Zavaritsky Institute of Geology and Geochemistry, <http://eng.igg.uran.ru>;
 Ural Federal University, <https://urfu.ru/en>;
 Institute of Metallurgy, <http://www.imet-uran.ru>.

References

- Frank M, Smetanin SN, Jelinek M, Vyhlihal D, Kopalkin AA, Shukshin VE, Ivleva LI, Zverev PG, Kubecek V. Synchronously-pumped all-solid-state SrMoO_4 Raman laser generating at combined vibrational Raman modes with 26-fold pulse shortening down to 1.4 ps at 1220 nm. *Opt Laser Technol.* 2019;111:129–133. doi:[10.1016/j.optlastec.2018.09.045](https://doi.org/10.1016/j.optlastec.2018.09.045)
- Künzel R, Umisedo NK, Okuno E, Yoshimura EM, de Azevedo Marques AP. Effects of microwave-assisted hydrothermal treatment and beta particles irradiation on the thermoluminescence and optically stimulated luminescence of SrMoO_4 powders. *Ceram Int.* 2020;46:15018–15026. doi:[10.1016/j.ceramint.2020.03.032](https://doi.org/10.1016/j.ceramint.2020.03.032)
- Yu H, Shi X, Huang L, Kang X, Pan D. Solution-deposited and low temperature-annealed $\text{Eu}^{3+}/\text{Tb}^{3+}$ -doped $\text{CaMoO}_4/\text{SrMoO}_4$ luminescent thin films. *Lumin J.* 2020;225:117371. doi:[10.1016/j.jlumin.2020.117371](https://doi.org/10.1016/j.jlumin.2020.117371)
- Elakkiya V, Sumathi S. Low-temperature synthesis of environment-friendly cool yellow pigment: Ce substituted SrMoO_4 . *Mater Lett.* 2020;263:127246. doi:[10.1016/j.matlet.2019.127246](https://doi.org/10.1016/j.matlet.2019.127246)
- Mikhailik VB, Elyashevskiy Yu, Kraus H, Kim HJ, Kapustianyk V, Panasyuk M. Temperature dependence of scintillation properties of SrMoO_4 . *Nucl Instrum Methods Phys Res A.* 2015;79:1–5. doi:[10.1016/j.nima.2015.04.018](https://doi.org/10.1016/j.nima.2015.04.018)

6. Danevich FA. Radiopure tungstate and molybdate crystal scintillators for double beta decay experiments. *Int J Mod Phys A*. 2017;32(30):1743008. doi:[10.1142/S0217751X17430084](https://doi.org/10.1142/S0217751X17430084)
7. Guo HH, Zhou D, Pang LX, Qi ZM. Microwave dielectric properties of low firing temperature stable scheelite structured (Ca,Bi)(Mo,V)O₄ solid solution ceramics for LTCC applications. *J Eur Ceram*. 2019;39:2365–2373. doi:[10.1016/j.jeurceramsoc.2019.02.010](https://doi.org/10.1016/j.jeurceramsoc.2019.02.010)
8. Yu-Ling Y, Xue-Ming L, Wen-Lin F, Wu-Lin L, Chuan-Yi T. Coprecipitation synthesis and photoluminescence properties of (Ca_{1-x}Y_x,Ln_y)MoO₄: xEu³⁺ (Ln = Y, Gd) red phosphors. *J Alloys Compd*. 2010;505:239–242. doi:[10.1016/j.jallcom.2010.06.037](https://doi.org/10.1016/j.jallcom.2010.06.037)
9. Xie A, Yuan X, Wang F, Shi Y, Li J, Liu L, Mu Z. Synthesis and luminescent properties of Eu³⁺-activated molybdate-based novel red-emitting phosphors for white LEDs. *J Alloys Compd*. 2010;501:124–129. doi:[10.1016/j.jallcom.2010.04.057](https://doi.org/10.1016/j.jallcom.2010.04.057)
10. Zhu Y, Zheng G, Dai Z, Zhang L, Ma Y. Photocatalytic and luminescent properties of SrMoO₄ phosphors prepared via hydrothermal method with different stirring speed. *J Mater Sci Techno*. 2017;33:23–29. doi:[10.1016/j.jmst.2016.11.019](https://doi.org/10.1016/j.jmst.2016.11.019)
11. Guo J, Randall CA, Zhou D, Zhang G, Zhang C, Jin B, Wang H. Correlation between vibrational modes and dielectric properties in (Ca_{1-3x}Bi_{2x}Φ_x)MoO₄ ceramics. *J Eur Ceram Soc*. 2015;35:4459–2264. doi:[10.1016/j.jeurceramsoc.2015.08.020](https://doi.org/10.1016/j.jeurceramsoc.2015.08.020)
12. Esaka T. Ionic conduction in substituted scheelite-type oxides. *Solid State Ionics*. 2000;136:1–9. doi:[10.1016/S0167-2738\(00\)00377-5](https://doi.org/10.1016/S0167-2738(00)00377-5)
13. Cheng J, Liu C, Cao W, Qi M, Shao G. Synthesis and electrical properties of scheelite Ca_{1-x}Sm_xMoO_{4+δ} solid electrolyte ceramics. *Mater Res Bull*. 2011;46:185–189. doi:[10.1016/j.materresbull.2010.11.019](https://doi.org/10.1016/j.materresbull.2010.11.019)
14. Fansuri H. Catalytic partial oxidation of propylene to acrolein: the catalyst structure, reaction mechanisms and kinetics[dissertation]. Perth (Australia): Curtin University of Technology; 2005. 191 p.
15. Sleight JAW, Aykan K. New nonstoichiometric molybdate, tungstate, and vanadate catalysts with the scheelite-type structure. *J Solid State Chem*. 1975;13:231–236. doi:[10.1016/0022-4596\(75\)90124-3](https://doi.org/10.1016/0022-4596(75)90124-3)
16. Guo J, Randall AC, Zhang G, Zhou D, Chen Y, Wang H. Synthesis, structure, and characterization of new low-firing microwave dielectric ceramics: (Ca_{1-3x}Bi_{2x}Φ_x)MoO₄. *J Mater Chem C*. 2014;2:7364–7372. doi:[10.1039/c4tc00698d](https://doi.org/10.1039/c4tc00698d)
17. Mikhaylovskaya ZA, Abrahams I, Petrova SA, Buyanova ES, Tarakina NV, Piankova DV, Morozova MV. Structural, photocatalytic and electroconductive properties of bismuth-substituted CaMoO₄. *J Sol State Chem*. 2020;291:121627. doi:[10.1016/j.jssc.2020.121627](https://doi.org/10.1016/j.jssc.2020.121627)
18. Mikhaylovskaya ZA, Buyanova ES, Petrova SA, Klimova AV. ABO₄ type scheelite phases in (Ca/Sr)MoO₄ - BiVO₄ - Bi₂Mo₃O₁₂ systems: synthesis, structure and optical properties. *Chimica Techno Acta*. 2021;8:20218204. doi:[10.15826/chimtech.2021.8.2.04](https://doi.org/10.15826/chimtech.2021.8.2.04)
19. Liang EJ, Huo HL, Wang Z, Chao MJ, Wang JP. Rapid synthesis of A₂(MoO₄)₃ (A = Y³⁺ and La³⁺) with a CO₂ laser. *Solid State Sci*. 2009;11:139–43. doi:[10.1016/j.solidstatesciences.2008.04.008](https://doi.org/10.1016/j.solidstatesciences.2008.04.008)
20. Porotnikova N, Khrustov A, Farlenkov A, Khodimchuk A, Partin G, Animitsa I, Kochetova N, Pavlov D., Ananyev M. Promising La₂Mo₂O₉-La₂Mo₃O₁₂ composite oxygen-ionic electrolytes: interphase phenomena. *ACS Appl Mater Interfaces* 2022;14:6180–6193. doi:[10.1021/acsami.1c20839](https://doi.org/10.1021/acsami.1c20839)
21. Chen Z, Bu W, Zhang N, Shi J. Controlled construction of monodisperse La₂(MoO₄)₃:Yb, Tm microarchitectures with upconversion luminescent property. *J Phys Chem C*. 2008;112:4378–83. doi:[10.1021/jp711213r](https://doi.org/10.1021/jp711213r)
22. Brazdil JF. Scheelite: a versatile structural template for selective alkene oxidation catalysts. *Catal Sci Technol*. 2015;5:3452–3458. doi:[10.1039/c5cy00387c](https://doi.org/10.1039/c5cy00387c)
23. Antonio MR, Teller RG, Sandstrom DR, Mehicic M, Brazdil JF. Structural characterization of bismuth molybdates by X-ray absorption spectroscopy and powder neutron diffraction profile analysis. *J Phys Chem*. 1988;92:2939–2944. doi:[10.1021/j100321a045](https://doi.org/10.1021/j100321a045)
24. Kubelka P, Munk FZ. Ein Beitrag zur optik der farbanstriche. *Techn Phys*. 1931;12:593–601.
25. Shannon RD. Revised effective ionic radii and systematic studies of interatomic distances in halides and chalcogenides. *Acta Cryst. A*. 1976;32:751–767. doi:[10.1107/S0567739476001551](https://doi.org/10.1107/S0567739476001551)
26. Vali R. Electronic properties and phonon spectra of SrMoO₄. *Comp Mater Sci*. 2011;50:2683–2687. doi:[10.1016/j.commatsci.2011.04.018](https://doi.org/10.1016/j.commatsci.2011.04.018)
27. Ramarao SD, Roopas Kiran S, Murthy VRK. Structural, lattice vibrational, optical and microwave dielectric studies on Ca_{1-x}Sr_xMoO₄ ceramics with scheelite structure. *Mater Res Bull*. 2014;56:71–79. doi:[10.1016/j.materresbull.2014.04.064](https://doi.org/10.1016/j.materresbull.2014.04.064)
28. Porto SPS, Scott JF. Raman Spectra of CaWO₄, SrWO₄, CaMoO₄ and SrWO₄. *Phys Rev*. 1976;157:716–719. doi:[10.1103/PHYSREV.157.716](https://doi.org/10.1103/PHYSREV.157.716)
29. Hardcastle FD, Wachs IE. Molecular structure of molybdenum oxide in bismuth molybdates by Raman spectroscopy. *J Phys Chem*. 1975;95:10763–10772. doi:[10.1021/j100179a045](https://doi.org/10.1021/j100179a045)
30. Jayaraman A, Wang SY, Shieh SR, Sharma SK, Ming LC. High-pressure Raman study of SrMoO₄ up to 37 GPa and pressure-induced phase transitions. *J Raman Spectrosc*. 1995;26:451–455. doi:[10.1002/jrs.1250260609](https://doi.org/10.1002/jrs.1250260609)
31. Salje EKH, Carpenter MA, Malcherek T, Boffa Ballaran T. Autocorrelation analysis of infrared spectra from minerals. *Eur J Mineral*. 2000;12:503–519. doi:[10.1127/0935-1221/2000/0012-0503](https://doi.org/10.1127/0935-1221/2000/0012-0503)
32. Pankrushina EA, Kobuzov AS, Shchapova YV, Votyakov SL. Analysis of temperature-dependent Raman spectra of minerals: Statistical approaches. *J Raman Spectrosc*. 2020;51:1549–1562. doi:[10.1002/jrs.5825](https://doi.org/10.1002/jrs.5825)
33. Verma A, Sharma SK. Rare-earth doped/codoped CaMoO₄ phosphors: A candidate for solar spectrum conversion. *Solid State Sci*. 2019;96:105945. doi:[10.1016/j.solidstatesciences.2019.105945](https://doi.org/10.1016/j.solidstatesciences.2019.105945)
34. Zhang Y, Holzwarth NAW, Williams RT. Electronic band structures of the scheelite materials CaMoO₄, CaWO₄, PbMoO₄ and PbWO₄. *Phys Rev B*. 1998;57:12738–12750. doi:[10.1103/PhysRevB.57.12738](https://doi.org/10.1103/PhysRevB.57.12738)
35. Mikhaylovskaya ZA, Pankrushina EA, Komleva EV, Ushakov AV, Streltsov SV, Abrahams I, Petrova SA. Effect of Bi substitution on the cationic vacancy ordering in SrMoO₄-based complex oxides: structure and properties. *Mater Sci Eng B*. 2022;281:115741. doi:[10.1016/j.mseb.2022.115741](https://doi.org/10.1016/j.mseb.2022.115741)
36. Maji BK, Jena H, Asuvathraman R, Kutty KVG. Electrical conductivity and thermal expansion behavior of MMoO₄ (M = Ca, Sr and Ba). *J Alloys Compd*. 2015;64:475–479. doi:[10.1016/j.jallcom.2015.04.054](https://doi.org/10.1016/j.jallcom.2015.04.054)
37. Irvine JTS, Sinclair DC, West AR. Electroceramics: characterization by impedance spectroscopy. *Adv Mat*. 1990;2:132–138. doi:[10.1002/adma.19900020304](https://doi.org/10.1002/adma.19900020304)
38. Vinke I, Diepgrond J, Boukamp B, de Vries KJ, Burggraaf AJ. Bulk and electrochemical properties of BiVO₄. *Solid State Ionics*. 1992;57:83–89. doi:[10.1016/0167-2738\(92\)90067-y](https://doi.org/10.1016/0167-2738(92)90067-y)
39. Hartmanova M, Le MT, Jergel M, SmatkoV, Kundracik F. Structure and electrical conductivity of multicomponent metal oxides having scheelite structure. *Rus J Electrochem*. 2009;45:621–629. doi:[10.1134/S1023193509060019](https://doi.org/10.1134/S1023193509060019)